3D DATA-DOMAIN REFLECTION TOMOGRAPHY FOR INITIAL VELOCITY MODEL BUILDING USING CHALLENGING 3D SEISMIC DATA

A. BAKULIN [1], I. SILVESTROV [1], D. NEKLYUDOV [2], K. GADYLSHIN [2] and M. PROTASOV [2]

[1] EXPEC Advanced Research Center, Saudi Aramco, Building 137, Dhahran 31311, Saudi Arabia. andrey.bakulin@aramco.com; ilya.silvestrov@aramco.com
[2] Institute of Petroleum Geology and Geophysics SB RAS, Academician Koptyug ave. 3, 630090 Novosibirsk, Russia. neklyudovda@ipgg.sbras.ru; gadylshinkg@ipgg.sbras.ru; protasovmi@ipgg.sbras.ru

(Received May 15, 2020: revised version accepted February 15, 2021)

ABSTRACT

Bakulin, A., Silvestrov, I., Neklyudov, D., Gadylshin, K. and Protasov, M., 2021. 3D data-domain reflection tomography for initial velocity model building using challenging 3D seismic data. *Journal of Seismic Exploration*, 30: 419-446.

We present a novel workflow to build a reliable initial velocity depth model from challenging seismic data. This workflow is based on automated 3D grid reflection tomography that utilizes coherent poststack and prestack reflection events in the data domain. The workflow consists of two parts: data preconditioning and nonlinear tomographic inversion. Data preconditioning is underpinned by robust data-driven prestack data enhancement in the form of 3D nonlinear beamforming. Operating directly in the data domain, we obtain robust NMO velocities and pick main reflection events on stacked time images. Ray-based tomographic inversion fits prestack traveltimes approximated by hyperbolae using the engine of standard grid reflection tomography.

Powerful prestack enhancement, combined with regularization of observed traveltimes by hyperbolae, delivers a robust and computationally efficient approach to reconstructing the velocity depth model directly in the data domain during the early stages of seismic processing. The new approach enables iterative depth processing critical for low signal-to-noise ratio data such as land seismic with small field arrays or single sensors. We present the tomographic workflow details and showcase the method's capabilities using synthetic and real data examples.

KEY WORDS: reflection tomography, inverse problem, land seismic data.

0963-0651/21/$5.00

INTRODUCTION

Estimation of the depth velocity model plays a vital role in the modern seismic data processing. Many approaches to tackle this problem have been proposed during the past decades (Robein, 2010). A classical solution is a reflection traveltime tomography. Gjoystdal and Ursin (1981) proposed one of the earliest 3D algorithms in which the model to be recovered is represented by a set of layers. Each layer is characterized by laterally varying velocity between continuous reflectors at the top and bottom of the layer. Velocity distribution in the layers and shape of the reflectors should be recovered by inversion of reflection traveltimes. The method requires picking of reflectors and corresponding reflection traveltimes that become an input data for tomography. The main challenge for such classical techniques is how to robustly extract kinematical information such as traveltimes of the reflected waves from complex, noisy wavefields in an automated way.

An effective alternative solution is provided by migration velocity analysis (MVA). Nowadays, it is often considered a standard practical method for depth velocity model building (Robein, 2010). In this method, the picking is automatically performed, but after the data are transformed into the depth domain by prestack depth migration (PSDM) with some initial velocity model. Modern MVA implementations make no assumptions on the reflections' continuity and operate with several independent reflection points in depth. By analyzing common-image gathers (CIGs) obtained during the migration of different data subvolumes, we can estimate traveltime residuals induced by inaccuracies in the initial velocity model. These residuals are used as input data for reflection traveltime tomography to update the initial velocity model. In essence, prestack depth migration inside MVA transforms the data into a better-conditioned (image) domain for traveltime tomography as compared to the classical algorithms. The disadvantage of MVA is the need to repeat computationally expensive and lengthy cycles of 3D prestack depth migration and perform re-picking at every nonlinear iteration of the velocity model update. To converge effectively, MVA requires starting from an adequate and good enough initial velocity model that provides coherent and focused CIGs for residual moveouts' picking.

Another approach operating directly in the data domain and allowing nonlinear tomography iterations without additional cycles of PSDM, is slope tomography or stereotomography (Billette and Lambaré, 1998; Lambaré, 2008). In this method, reflected events are described as coherent local events in prestack data. The events' traveltimes and slopes are obtained from the observed data by automated picking. Together with the known positions of source and receiver, these quantities serve as inputs to estimate the unknown velocity model. The reliable picking of all local coherent events' attributes required for tomography in noisy prestack data is quite challenging, especially on land. To overcome this issue and to provide more reliable data for stereotomography, several approaches have been proposed. In poststack

stereotomography, estimated kinematic parameters from a common-reflection surface (CRS) method are utilized to derive the local kinematic attributes (Lavaud et al., 2004). The CRS method uses global approximation, meaning that its kinematic parameters are estimated at zero offset using a subset of data with a wide range of offsets and midpoints. Hence, it can provide more robust but less resolved attributes' estimation. The resolution may be improved by residual stereotomography (Neckludov et al., 2006), which deals with data traces and may be very computationally expensive in 3D. Both of these approaches rely on the use of stereotomography inversion engine and can be considered as a data preparation procedure for stereotomogaphy. Another approach related to poststack stereotomography is normal-incidence-point (NIP) tomography proposed by Duveneck (2004), where global kinematic parameters from the CRS method are directly used for inversion. These parameters are the traveltimes themselves, their second-order derivatives, and the lateral positions of the attributes picked from CRS stack sections. As in poststack stereotomography, picking is facilitated in the poststack data domain with its higher signal-to-noise ratio. Since only locally coherent events are considered, no assumptions are required about interfaces' continuity, and no interpretation of events is necessary. Both NIP-tomography and stereotomography have been implemented as grid tomographic approaches. An extensive comparison of these methods may be found in Dümmong et al. (2008).

To combine the flexibility of the original prestack stereotomography and robustness of picking in the migrated domain, an approach based on kinematic invariants has been introduced (Chauris et al., 2002; Guillaume et al., 2008; Lambaré et al., 2014). The coherent local events are picked in depth- or time-migrated domains. They are then demigrated back to the data domain using the same reference velocity model as for the original migration. This provides the input data required for stereotomography, and closes the loop between stereotomography and MVA methods. So it is a powerful tool for velocity model building that does not require multiple cycles of PSDM; it is a relatively sophisticated method. Similar to NIP-tomography, it needs computationally expensive dynamic ray tracing. Both of them rely on the sensitivity matrices explicitly built from the paraxial quantities, which are quite complex in both cases. This might lead to a computational burden when massive 3D data sets are processed. One more drawback of this approach results from a misfit function containing several terms of different nature and dimensions such as traveltimes and their first- and/or second-order derivatives. Such hybrid misfit function requires a very careful choice of regularization parameters. It can otherwise lead to poorly conditioned inversion with unreliable results.

This paper proposes a simplified but more computationally efficient reflection tomography algorithm that does not require cycles of PSDM and re-picking. Our approach is based on kinematic attributes, which are readily available at the early stages of seismic processing, namely stacking

velocities. We are also using coherent local events from the stacked volume, picked automatically together with their corresponding dips. They probably represent the most robust kinematical and structural parameters obtained from seismic data early in the processing flow. The presented method uses only traveltime residuals between observed and synthetic data in the misfit function. It can be implemented using only conventional kinematic ray tracing and tomographic inversion algorithms. Since the kinematics of the travelitmes in the observed data is approximated by the stacking velocities, the method has similarities with the previous velocity inversion approaches (Rakotoarisoa et al., 1995; Guiziou et al., 1996; Sexton, 1998; Sexton and Williamson, 1998). However, it does not require interpretation of the horizons. It can be considered an automatic extension of these algorithms based on grid tomography's current industry best practice. The main approximation of our approach is the usage of hyperbolic moveout approximation. If the prestack data quality allows, this approximation can be relaxed by introducing more elaborate representation of input traveltimes, for example arising from using local prestack kinematic attributes etc. In summary, more complex traveltime approximations can be easily incorporated using the same framework.

The proposed method's primary intent is to retrieve initial velocity models for noisy land and marine data earlier in the processing flow. Other methods of initial model building often struggle with challenging prestack data quality. At the same time, the success of the computationally demanding procedures such as MVA, stereotomography, or full-waveform inversion hinges on the quality of the initial model. To mitigate the data quality challenge, enhancement of the prestack data before tomographic inversion is essential. Data-driven enhancement techniques based on multi-dimensional local stacking of neighboring traces are very effective for this purpose (Baykulov and Gajewski, 2009; Buzlukov and Landa, 2013; Xie, 2017; Berkovitch et al., 2011, Rauch-Davies et al. 2013; Bakulin et al., 2018a,b, 2020). Notably, a nonlinear beamforming algorithm improves stacking velocity analysis results and the quality of stack volumes (Bakulin et al., 2018a,b, 2020). Furthermore, the same algorithm can estimate the coherent local events and their dips from the enhanced stacks to form the input data for the proposed tomography.

The content of the paper is as follows. First, we present the proposed tomographic workflow and describe in more detail each step of the algorithm. We also cover some implementation details of the developed software code. Next, we present a realistic 3D synthetic example from the area with the salt intrusion. Finally, we show field examples using a marine ocean-bottom-cable seismic dataset.

TOMOGRAPHIC WORKFLOW

Any traveltime tomographic approach can be decomposed into two main parts: calculation of traveltime residuals between observed and simulated arrivals and inversion of traveltime residuals. This paper proposes a novel way to prepare the observed traveltimes and other input data for 3D data with a low signal-to-noise ratio. At the same time, the inversion itself is based on a well-established industry workflow for reflection grid tomography. The workflow is divided into two parts: data preparation and nonlinear tomographic inversion. Required inputs are prestack 3D seismic data and the initial depth velocity model, whereas the output is the final updated depth velocity model. Fig. 1 summarizes the new workflow, and below, we describe it in detail.

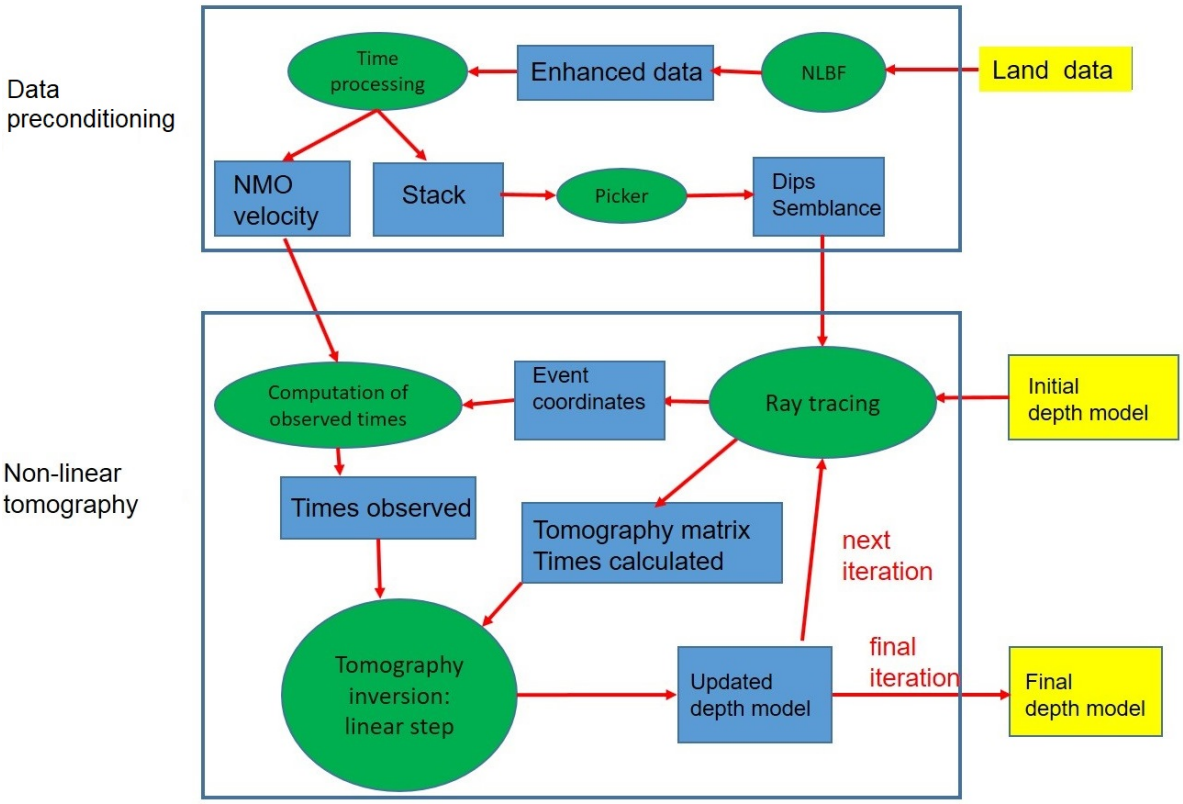

Fig. 1. Schematic workflow for 3D data-domain reflection tomography.

Part I: Data preparation

Input for this part is 3D prestack seismic data volume. Since we target data with low SNR at the early stages of time processing, this step requires a

robust data-driven enhancement procedure capable of significantly increasing SNR to enable:

- automatic NMO velocity estimation providing reliable stacking velocities,
- stacked time image of enhanced data exhibiting locally coherent events that could be reliably picked.

The data preparation step's output is the NMO velocity cube, and semblance and estimated dips picked on the stacked image. Let us describe the main stages in detail.

Stage 1: prestack seismic data enhancement

We select nonlinear beamforming or NLBF (Bakulin et al., 2018a,b, 2020) as the primary pre-conditioning step applied to the original 3D prestack seismic data. The main idea behind NLBF is to collect signals from neighboring traces along locally defined surfaces that follow the local moveout of coherent seismic signals. Parameters that describe these surfaces may be treated as local wavefront attributes of reflected waves and are estimated directly from the data (Bakulin et al., 2020). These parameters are dips and curvatures of seismic wavefronts in specific directions in the acquisition plane. We find 3D data enhancement particularly useful in the cross-spread domain for modern land and OBC orthogonal acquisition geometries (Bakulin et al., 2020). In this case, only five local kinematical parameters are estimated on a coarse grid to improve the method's efficiency. After this, local summation along the defined local traveltime surfaces is performed. As a result of this stage, an enhanced dataset is obtained, satisfying the requirements of the data preparation step outlined above. We emphasize that an increase in SNR is especially dramatic for land seismic data acquired with single sensors or small field arrays. Such land data before enhancement is usually unable to deliver the required outputs for robust tomographic inversion.

Stage 2: obtaining inputs for data-domain nonlinear tomography

Enhanced prestack data serve as an input to the next step of estimating stacking velocities (V_{NMO}) and poststack attributes (times and slopes) required for data-domain tomography. A cube of NMO velocities is obtained using conventional velocity analysis. Since we are using the enhanced data with significantly increased SNR, estimation of V_{NMO} becomes more reliable than when velocity analysis is performed using the original field data (Bakulin et al., 2018b, 2020). A 3D CMP stack volume for time and slope picking is also constructed using the enhanced data with better SNR and

improved event continuity. Whereas stacked volumes can be enhanced by other methods, such as structurally-oriented filters (Fehmers and Höcker, 2003), NLBF in a single run delivers both enhanced stack and prestack data with improved SNR. Local coherent events are picked automatically within the 3D CMP stack volume, similarly to Duveneck (2004). The picking algorithm searches for such events in the CMP stack volume using maximum semblance criteria. Suppose the semblance value calculated in a current point is more than a predefined threshold. In that case, the point is considered as an actual local reflected event or "pick." Each accepted pick is associated with a normal ray. A pick is characterized by:

a) coordinates on the acquisition plane, X_{CMP}, Y_{CMP},

b) the two-way traveltime along the normal ray, T_0,

c) local slopes in inline and crossline directions DIP_X, DIP_Y which can be recalculated into normal ray's emergence angles γ_X, γ_Y in inline X-direction, and crossline Y-direction, using the expression $DIP_{X,Y} = \frac{\sin \gamma_{X,} \gamma_Y}{V}$ where V is the initial velocity at the point (X_{CMP}, Y_{CMP}) on the acquisition surface (Hubral and Krey, 1980).

Picking can be conveniently done using the nonlinear beamforming algorithm itself (Bakulin et al., 2020) applied to poststack data or other suitable techniques. As a result of this stage, a collection of independent picks describing strong reflected events are obtained in the 3D poststack data domain.

Part II: Data-domain nonlinear tomographic inversion

Inputs for the second part of the tomographic workflow are volume of NMO velocities, initial depth velocity model, and volume of picks, i.e., dips and semblances estimated on the stack. The output is the final updated velocity model in depth. Nonlinear tomography inversion contains several linear steps. Each step consists of three stages: generation of synthetic traveltimes with ray tracing in the initial depth velocity model, estimation of observed traveltimes, and linear tomographic inversion. Since original picks were obtained from the 3D CMP stack volume, the first stage localizes them into the depth domain using top-down normal ray tracing. Then bottom-up ray tracing from the depth picks is performed to compute traveltimes in the current velocity model and form a tomography matrix. The second stage estimates observed traveltimes using a hyperbolic approximation. In the third stage, an actual linear traveltime inversion is performed, and the initial depth model is updated. These three stages are repeated iteratively to improve the fit and arrive at the final depth model. Let us describe them in more detail.

Stage 1: generation of synthetic traveltimes using ray tracing

Modeled traveltimes are generated in two steps. First, we localize or "move" the picks to the depth image domain. Then, we ray trace from the pick location in depth until we hit the acquisition surface to obtain synthetic traveltimes and form a tomography matrix.

Stage 1.1: localization of picks in depth using normal ray tracing

Each accepted pick is localized in depth using zero-offset ray tracing using the initial depth velocity model (Fig. 2a). As we mentioned above, each pick is characterized by five parameters: $X_{CMP}, Y_{CMP}, T_0, \gamma_X, \gamma_Y$. For each pick, an associated normal ray is traced in the initial velocity model starting from the point (X_{CMP}, Y_{CMP}) at the acquisition surface with the emergence direction defined by the angles γ_X, γ_Y. The normal ray is traced in the inhomogeneous initial velocity model until time $T_0/2$ has been reached (Fig. 2a). The normal ray's final point defines a position (X, Y, Z) and orientation given by a normal vector $\vec{N}$ of the local reflection surface at depth in the current velocity model (Hubral and Krey, 1980; Gjoystdal and Ursin, 1981). All elementary reflection surfaces in depth are assumed to be independent.

Stage 1.2: synthetic offset traveltimes obtained by bottom-up offset ray tracing

Each pick in depth defines a local reflection surface described by its position (X, Y, Z) and normal vector $\vec{N}$. A fan of reflected rays emerging from the reflection surface is traced towards the acquisition surface. Each reflected ray consists of two segments satisfying Snell's law at the reflection's surface (see Fig. 2b). We trace multiple rays from depth by incrementally varying the reflection angles and azimuths. The reflected rays arrive at the acquisition surface at two locations that can be considered "virtual" source and receiver. These terminations points of each reflected ray at the acquisition surface may be uniquely defined by the midpoint coordinate X_{CMP}, Y_{CMP}, absolute offset h (distance between the source and receiver), and azimuth α. Traveltime along each reflected ray is computed in the initial model. Traveltimes $T_{CALC} = T_{CALC}(X_{CMP}, Y_{CMP}, h, \alpha)$ are calculated along the reflected rays emerging from the same elementary reflection surface and forming a common reflection-point traveltime surface

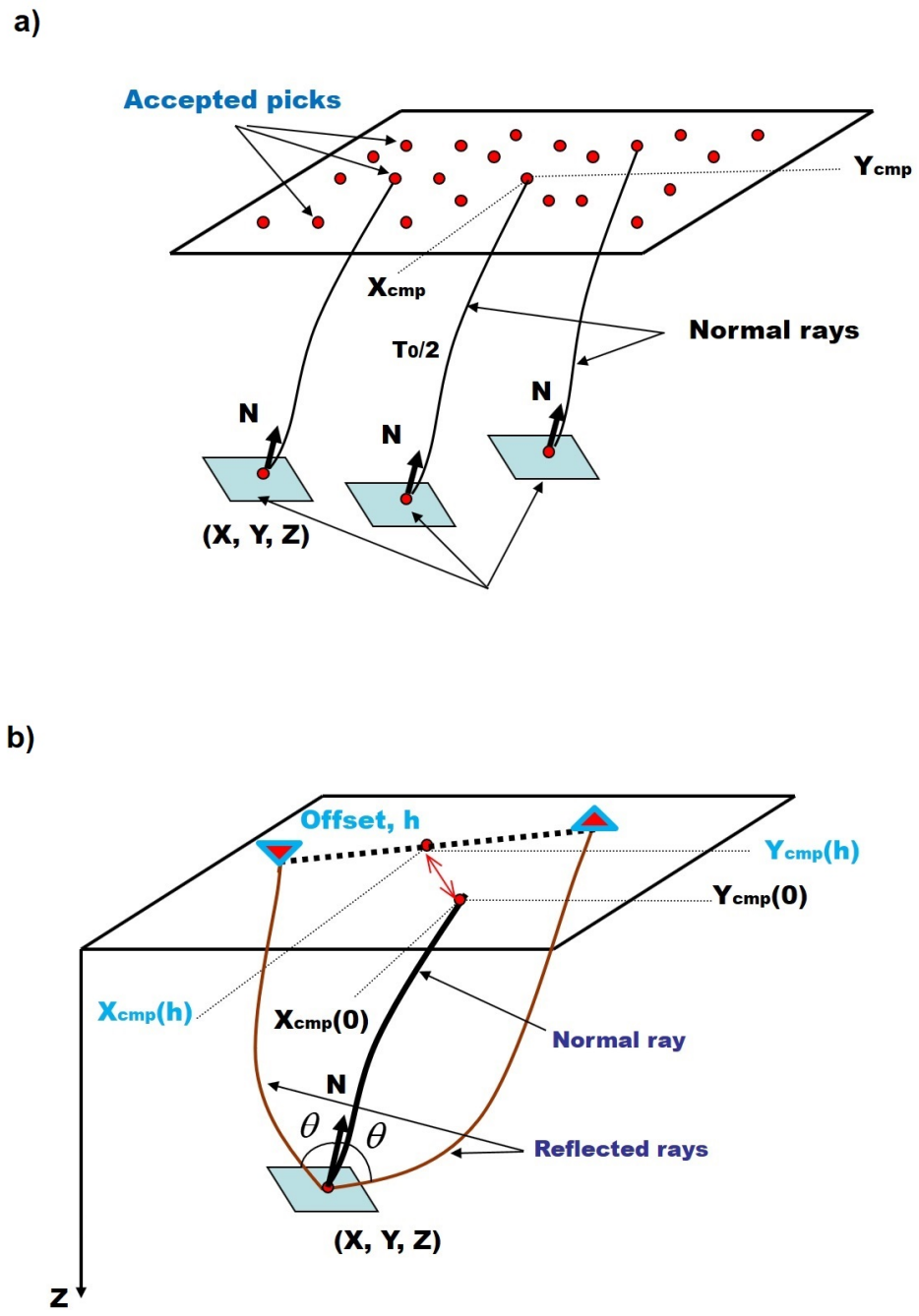

Fig. 2. Localization of the picks in depth using normal ray tracing (a) and generating synthetic offset traveltimes using bottom-up offset ray tracing (b).

in the data space. Note that in the true model, two segments of each reflected ray will be centered around the corresponding zero-offset ray, with a surface CMP location being at the center of the offset vector. However, this would not be the case in the erroneous model. The CMP location may be shifted away from the offset vector shown in Fig. 2b. Computed traveltimes T_{CALC} along with the associated coordinates of source and receiver, and zero-offset traveltimes allow us to form a tomography matrix M. The velocity model is parametrized by a 3D regular grid with constant speed inside each voxel. M_{ij} denotes a length of i-th reflected ray within j-th voxel. So we arrive at a classical "grid" tomography problem (Jones, 2014). Each pick corresponds to a block of rows in the matrix M. The size of M in the isotropic case is $N_{Rays} \cdot N_X \cdot N_Y \cdot N_Z$, where N_{Rays} is a number of successfully constructed reflected rays, whereas $N_X \cdot N_Y \cdot N_Z$ is total count of points in the subsurface velocity grid. In a typical case, the number of rows significantly exceeds the number of columns.

Stage 2: estimation of observed traveltimes

In this stage, we approximate observed experimental traveltimes using conventional hyperbolic approximation:

$$T_{OBS}(X_r, Y_s, X_s^*, Y_r^*) = T_{NMO}(X_r, Y_s, X_s^*, Y_r^*), \quad (1)$$

where T_{NMO} describes normal moveout defined by NMO velocities estimated after prestack enhancement with NLBF:

$$T_{NMO} = \sqrt{T_0^2 + h^2/V_{NMO}^2}. \quad (2)$$

Here T_0 is zero-offset two-way traveltime of the pick, $h = \sqrt{(X_r - X_s^*)^2 + (Y_r^* - X_s)^2}$ is an offset of the point where "observed" common-reflection-point traveltime is estimated, whereas $V_{NMO} = V_{NMO}(X_{CMP}, Y_{CMP}, T_0)$ is NMO velocity used for moveout corrections at the current midpoint.

More sophisticated approximations may be used here (for example, 4th order approximation described by Al-Chalabi (1973) and Alkhalifah (1997)). Note that NMO velocity may be additionally azimuthally dependent (Yilmaz, 2001).

Proper CMP attributes (V_{NMO} and T_0) need to be identified for given reflected rays according to eq. (2). Let us consider the picked point in the

stack volume with coordinates $X_{CMP}(A), Y_{CMP}(A)$ at the surface (Fig. 3). The normal ray traced in the current velocity model provides the reflection point A and the corresponding local reflection surface associated with it. Reflected rays emerging from this point arrive back to the acquisition surface with midpoint coordinates $X_{CMP}(B), Y_{CMP}(B)$. If this midpoint is located within the same bin as the original midpoint $X_{CMP}(A), Y_{CMP}(A)$, then the corresponding CMP attributes are used. Otherwise, we use the local slope (and curvature, if available) calculated during the zero-offset picking to construct the local zero-offset traveltime surface associated with this coherent event. Projection of point $X_{CMP}(B), Y_{CMP}(B)$ onto this surface provides corrected normal two-way traveltime $T_0(B)$ and corresponding NMO velocity. When the two midpoints are far away from each other, the pick is dropped from the inversion during the current iteration.

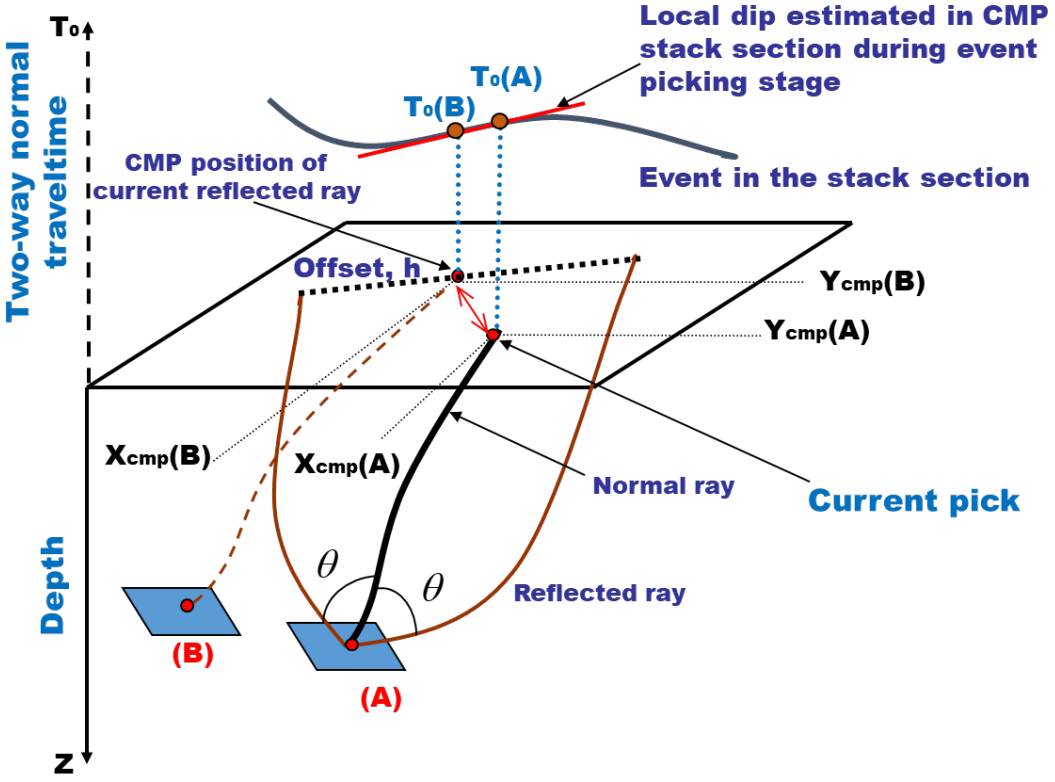

Fig. 3. Proper identification of CMP attributes for reflected ray.

While such approximated traveltimes may not perfectly describe actual moveout, they represent a fit-for-purpose and stable approximation for challenging data that is critical in tomographic inversion. Data-domain tomography requires estimation of prestack reflection traveltimes that is hard to achieve on noisy land data. Using NMO hyperbolas estimated on

enhanced data to approximate the observed traveltimes is equivalent to regularization of traveltimes. Such regularization leads us to a stable solution for the macro-velocity model at the cost of losing some details at smaller scales. We believe such regularization is an acceptable compromise for the initial velocity model building. The more refined representation can be achieved by other methods such as common-image point tomography, migration velocity analysis, or full-waveform inversion. To better estimate the actual reflection traveltimes at exit points of calculated reflected rays, it is also possible to use wavefront attributes obtained during the data enhancement stage with NLBF.

Stage 3: traveltime inversion – solution of the linearized inverse problem

Now that we obtained both observed (T_{OBS}) and modeled (T_{CALC}) reflection travel-times, we can form traveltime residuals for each emergence point of reflected rays:

$$dT(X_{CMP}, Y_{CMP}, h, \alpha) = T_{OBS}(X_{CMP}, Y_{CMP}, h, \alpha) - T_{CALC}(X_{CMP}, Y_{CMP}, h, \alpha). \quad (3)$$

These residuals serve as input for a conventional 3D reflection grid tomography algorithm, for example, similar to the one described by Woodward et al. (2008). However, we note that our approach may be used with any other 3D inversion tomography engine. From tomographic inversion, a newly updated initial velocity model is obtained. Ray tracing, event localization, and linear inversion stages are iteratively repeated until an acceptable misfit between the calculated and actual traveltimes is reached.

To solve a linearized inverse kinematic problem, a tomographic system of linear algebraic equations (SLAE) is constructed during the ray tracing stage. Tomographic SLAE forms a linear relationship between traveltime residuals dT and desired model update vector Δv

$$M\Delta v = dT \quad . \quad (4)$$

Here M is a tomographic matrix with the elements representing derivatives of reflection traveltimes with respect to model parameters described above.

Below we follow an approach proposed by Woodward et al. (2008). Instead of the original linear system (4), a pre-conditioned system is solved:

$$LMSR\Delta v' = LdT \quad , \quad (5)$$

where L is a diagonal weighting matrix of rows, R is a diagonal weighting matrix of columns, S is a spatial smoother (which acts as a 3D convolution with a triangle function).

Pre-conditioned system (5) is solved using the Iterative Reweighted Least-Squares (IRLS) method (Scales et al. 1988) with norm $L_{1.5}$ (Woodward et al., 2008). In this case, the cost function which is minimized during the solution of the inverse problem may be expressed as

$$F = \|LMSR\Delta v' - LdT\|_{1.5}^{1.5} + \lambda^2\|\Delta v'\|_2^2 = \left\|A\vec{x} - \vec{b}\right\|_{1.5}^{1.5} + \lambda^2\|\vec{x}\|_2^2. \quad (6)$$

Where notations $A = LMSR$, $\vec{x} = \Delta v'$, $\vec{b} = LdT$ are used.

The inverse problem comes down to solving the set of typical least-squares problems with a recursively updated matrix of weights

$$A^T W_{k-1} A\overrightarrow{x_k} = A^T W_{k-1}\vec{b}\ . \quad (7)$$

Here diagonal weighting matrix W_k at k-th IRLS iteration is determined as $W_k = diag|r_i|^{-0.5}$, where $r_i = \sum A_{ij} - b_i$ is a residual vector after *(k-1)*-th iteration. SLAE's (7) is solved using the LSQR method (Paige and Saunders, 1982) typical for tomographic applications. The solution of the tomographic system (5) with the help of IRLS allows us to obtain solutions that are much more stable to abrupt "jumps" of input data (outliers). Outliers' impact on the final solution is a significant challenge in tomographic problems when solving them by the standard least-squares method.

It is important to highlight key features of SLAE's arising in seismic tomography that are important for the chosen realization of the code: 1) Huge dimensions of the system of equations (> 10^6 equations with more than 10^8 unknowns); 2) Matrix is very sparse with a relatively small number of nonzero elements (~1-3 %); 3) Problem is ill-posed demanding usage of pre-conditioning and regularization procedures. For real-world applications, gigabytes of memory are needed to operate with such matrices (even considering their sparsity). Therefore, software implementation of 3D tomography should be initially focused on using high-performance computing systems with distributed memory (MPI - implementation). Our tomography implementation is based on using the functionality in the freeware library PETSc (http://www.mcs.anl.gov/petsc). The PETSc library is oriented explicitly for coding MPI-oriented programs that extensively use elements of linear algebra. PETSc has the following advantages: 1) It contains a set of MPI-oriented iterative algorithms for solving SLAE such as LSQR; 2) It is suitable for working with data arrays distributed over computing nodes (matrices, vectors) and performing any operations with

such objects; 3) It provides a convenient way to deal with sparse matrices distributed over nodes.

Following Woodward et al. (2008), the model update's pre-conditioning based on triangular smoothing has been implemented in the code. Smoothing is carried out as a 3D spatial convolution with triangular functions. There are two possible strategies for smoothing.

The first strategy is "multiscale" smoothing. For each linearized inverse problem, we attempt to resolve many scales progressing from large to small using a fixed framework of a single linearized inverse problem. Then we apply similar "multiscale" smoothing inside all other linear iterations. Let's describe the main concept of the multiscale approach briefly. Initial problem (5) is represented as a series of the problems with "k" smoother S scales,

$$\sum_{k=1}^{N_S}[LMS_kR]\,\Delta v_{k-1} = d\ . \tag{8}$$

At the first "multiscale" iteration, $k = 1$, one fixes the biggest smoother apertures and solve the system using the IRLS method:

$$[LMS_1R]\Delta v_1 = d\ . \tag{9}$$

When the "long-wavelength" solution Δv_1 is obtained, the smoother aperture is decreased, and the linearized system at the next scale is solved:

$$[LMS_2R]\Delta v_2 = d - [LMS_1R]\Delta\widehat{v_1} = d_2. \tag{10}$$

This stage is repeated for each given smoother scale. Note that event positions remain fixed within the current velocity model, i.e., tomographic matrix M is the same during all iterations with different smoother aperture:

$$[LMS_3R]\Delta v_3 = d - [LMS_2R]\Delta\widehat{v_2} = d_3. \tag{11}$$

This classical "multiscale" approach is proven efficient in MVA applications (Woodward et al. 2008). The remigration stage is very computationally expensive because 3D PSDM and RMO picking must be redone for each updated velocity model.

The second strategy is "individual" smoothing for each linearized inverse problem. We resolve only a specific scale of velocity variation within one solution of a single linearized inverse problem. At the same time, the smoothing aperture can vary for other linear iterations. The second approach consists of solving the system (9) with a fixed "individual"

smoothing aperture at each linear iteration. In this case, matrix M is recalculated once again after each iteration, and we apply a new smoother aperture. In this case number of smothers, apertures equal the number of nonlinear iterations.

For our approach, where the remigration stage is relatively cheap, the second approach is the most efficient way to solve the problem. Of course, the multiscale approach may also be used. We implemented the multiscale approach and used it in all examples in this paper.

CASE STUDIES

Synthetic example: a realistic model with salt intrusion and field acquisition geometry

The first example is synthetic data corresponding to a real 3D case study shown later. The field case inspires the depth velocity model with the salt body shown in Fig. 4. Likewise, the acquisition geometry used for finite-difference simulation replicates the field case (Fig. 5). The total size of the depth model is 6,000 x 6,000 x 8,000 m. The model's discretization is 241x241x676 (X, Y, Z) points with spacings hz = 12 m and hx = hy = 25 m, respectively.

To check the reconstructed velocity model's reliability, we need to construct depth images and corresponding common-image gathers using Kirchhoff depth migration. CDP gathers corresponding to one CDP line have been extracted from the entire 3D dataset (Fig. 5). The whole ensemble of extracted CDP gathers has bins located along one inline direction, although individual traces in gathers are collected from different azimuths.

To obtain inputs required for tomography, our 3D tool for picking coherent local events has been applied to a stack section shown in Fig. 6. The volumetric distribution of semblance maxima is displayed in Fig. 7. Semblance maxima follow main coherent events as expected. Figs. 8 and 9 reveal corresponding inline (dip-x) and crossline (dip-y) dips of poststack local coherent events. We applied the semblance threshold of 0.6, passing only the most energetic reflection events to the inversion.

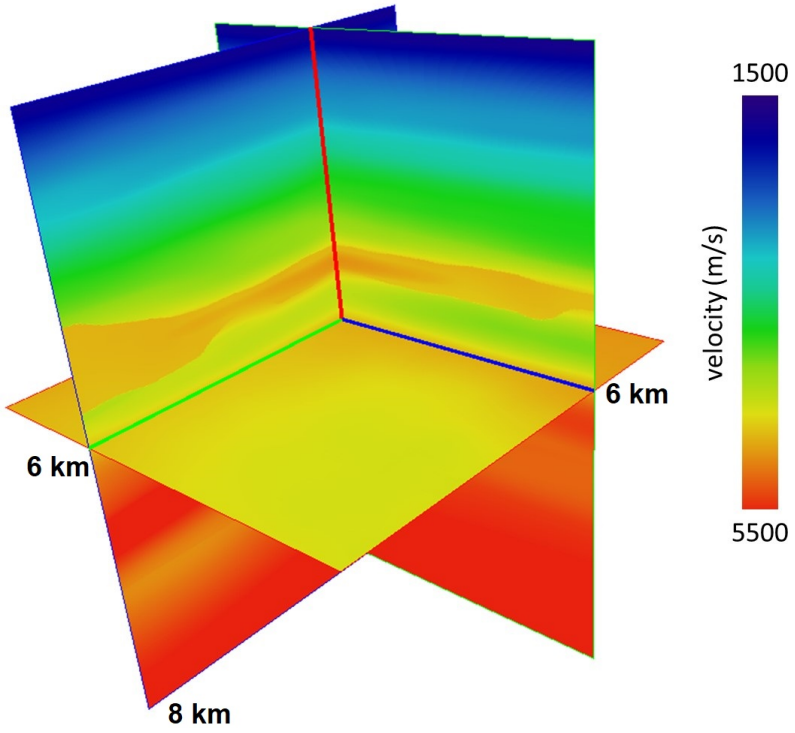

Fig. 4. The true 3D velocity model used for modeling the synthetic dataset.

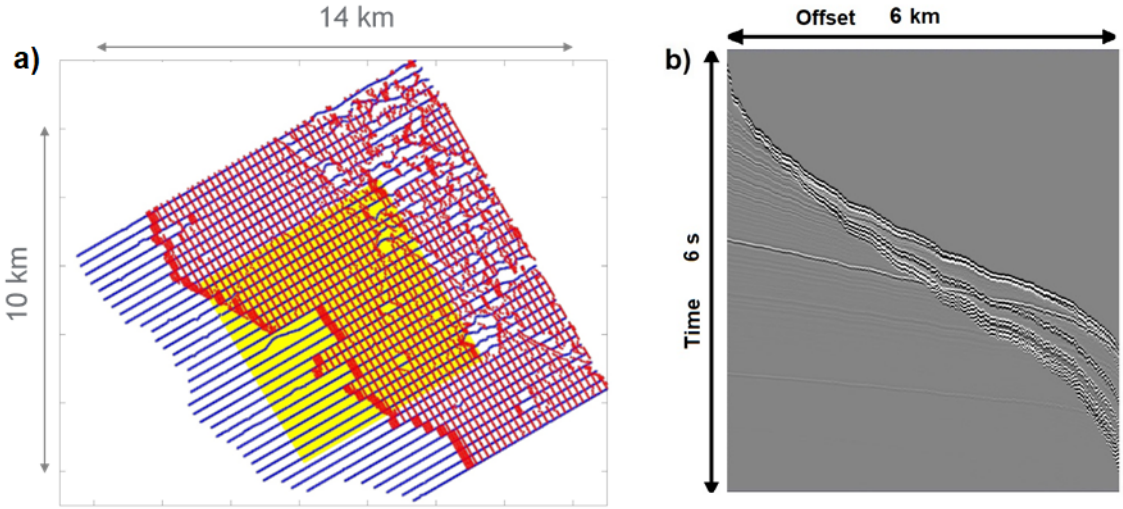

Fig. 5. (a) Acquisition geometry used for the synthetic case study: shots are marked by red dots, whereas blue dots denote receivers. The field case study inspires this geometry. (b) Typical CDP gather.

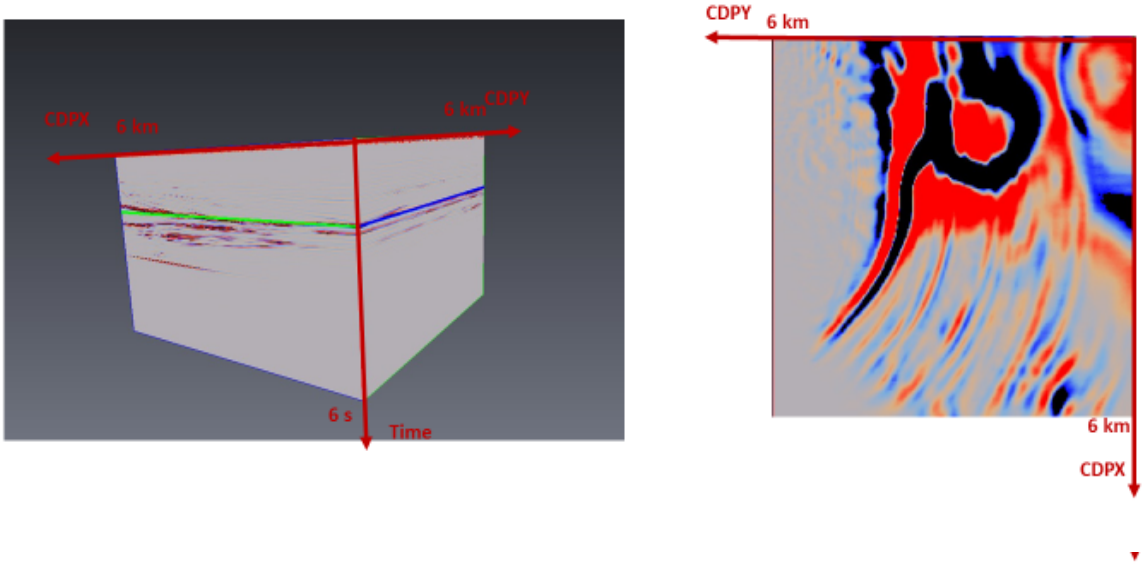

Fig 6. 3D view of the original stack section (left) used to pick local coherent events and time slice at t = 1.86 s (right).

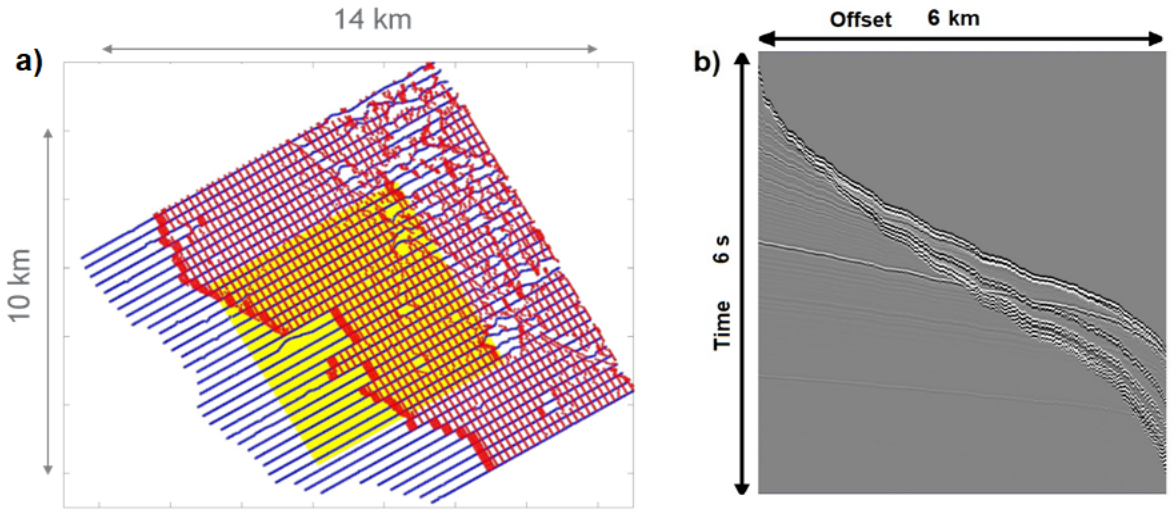

Fig. 7. 3D view with the volumetric distribution of semblance maxima (left) after picking coherent local events on the stack section and time slice at t = 1.86 s (right).

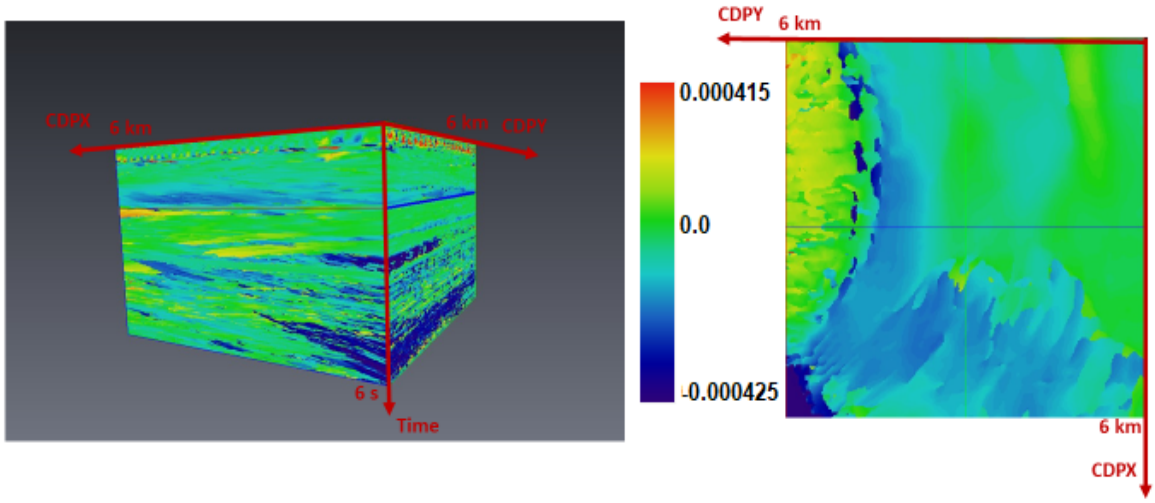

Fig. 8. Volumetric distribution of the inline dip (dip-x, left) estimated from the original stacked cube and time slice at t = 1.86 s (right).

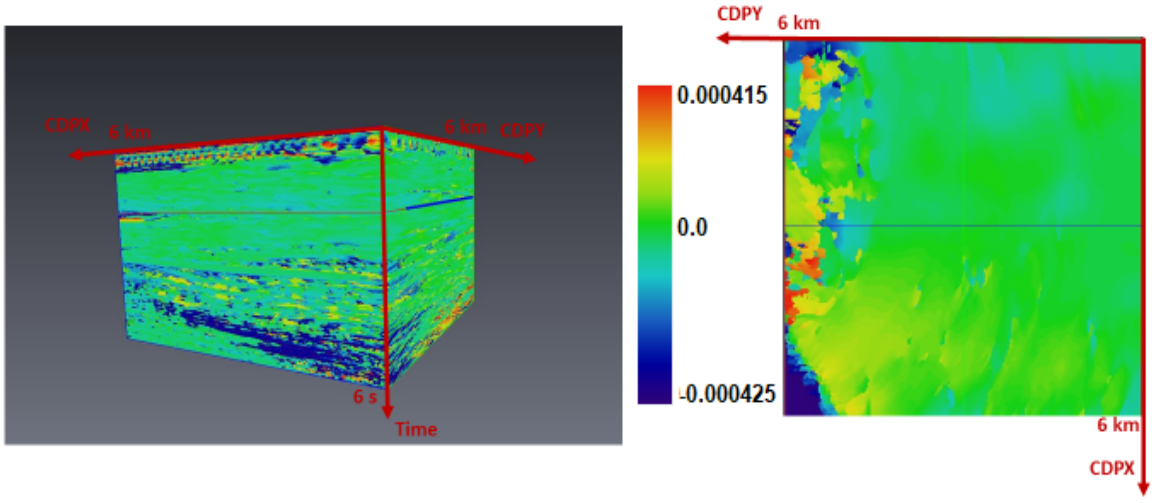

Fig. 9. Volumetric distribution of the crossline dip (dip-y, left) estimated from the original stacked cube and time slice at t = 1.86 s (right).

Input parameters of inversion were as follows: inversion grid discretization is Z_{cube}= 50 m, X_{cube} = Y_{cube}= 200 m. One fixed smoother loop was used with apertures of X = Y = 2000 m, Z = 500 m. The number of LSQR iterations is 20, whereas the number of IRLS (outer) iterations is equal to 10. The results after five nonlinear global iterations are presented in Fig.10b.

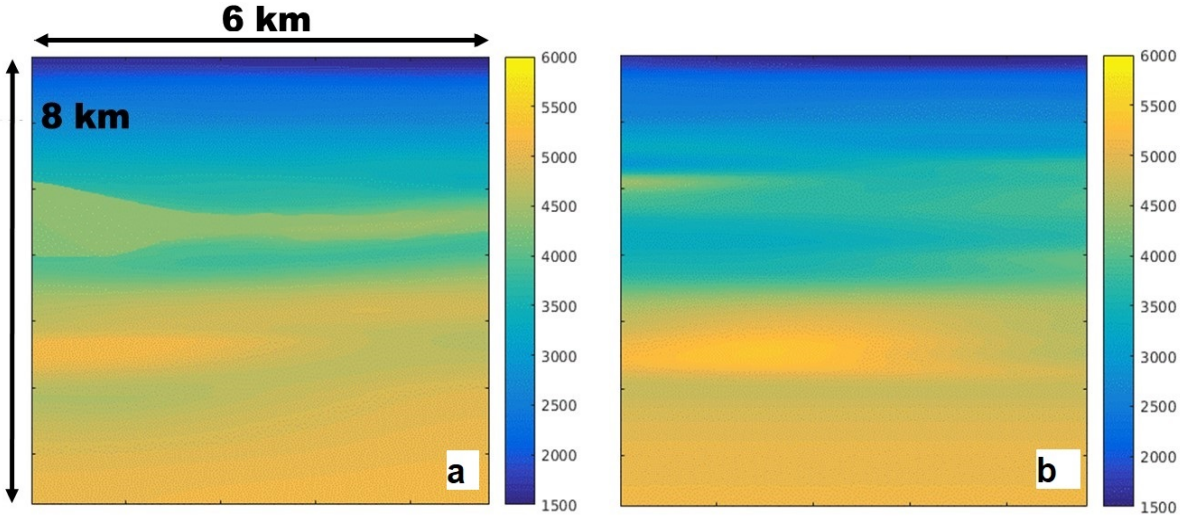

Fig. 10. (a) 2D slice through the exact velocity model in the middle of the cube; (b) Same 2D slice but after tomographic inversion.

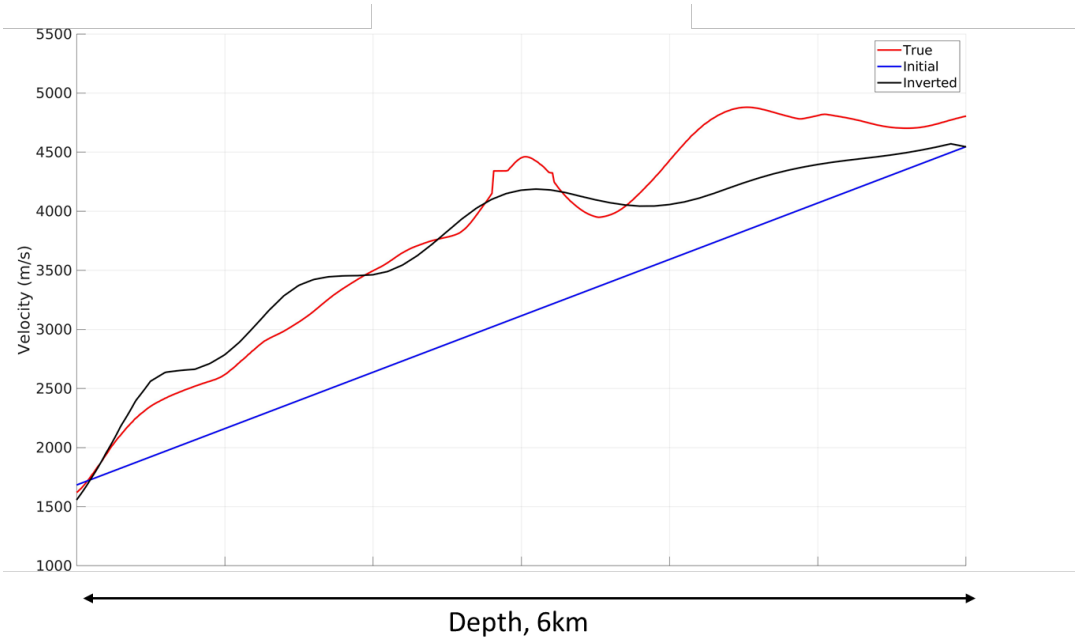

Fig. 11. Comparison of 1D velocity profiles extracted from the volume at X = 3000 km: true migration velocity profile (red), initial velocity model (blue), and inverted velocity model (black).

The 1D velocity profile was chosen as the initial velocity model (Fig. 11, black curve). It is a combination of two linear functions following the main velocity trends within a corresponding depth interval.

In this example, we could only migrate 3D data with Kirchhoff migration. So we limit maximum offsets used PSDM to a 4000 m maximum. Common-image gathers and depth images obtained after PSDM in the "true", initial and inverted models are presented in Figs. 12 and 13, respectively. Comparing the sections, we conclude that the image constructed with the recovered velocity model demonstrates a flattening of the reflected events on common-image gathers and more accurate positioning of the three primary reflectors of interest. For example, the deepest horizon located at the depth ~6000 m in the "true" image is mispositioned in the initial velocity model. In contrast, in the recovered model, it is more accurately placed.

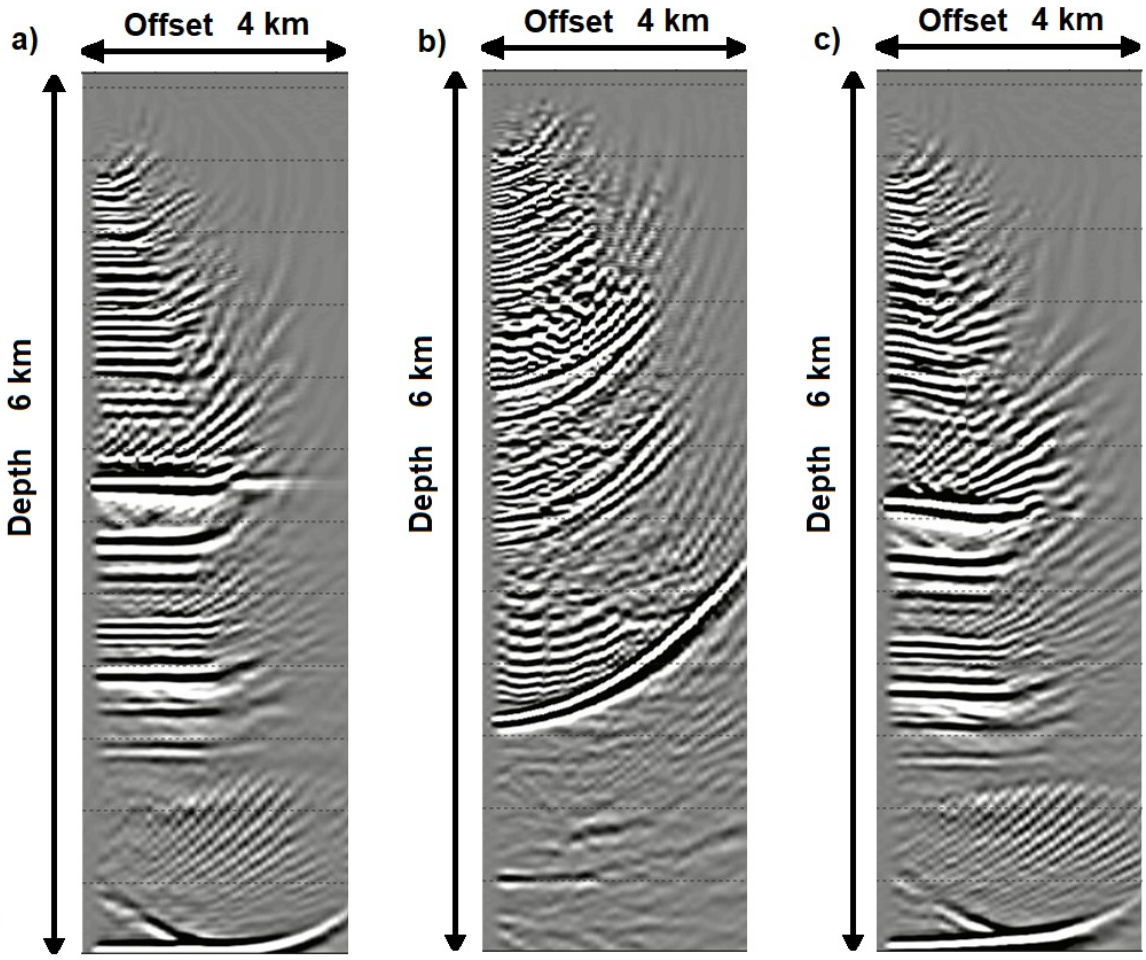

Fig. 12. Common-image gathers obtained with PSDM using: (a) the exact velocity model; (b) the 1D initial velocity model; (c) the recovered velocity model obtained by tomography. A maximum offset of 4000 m was used in migration.

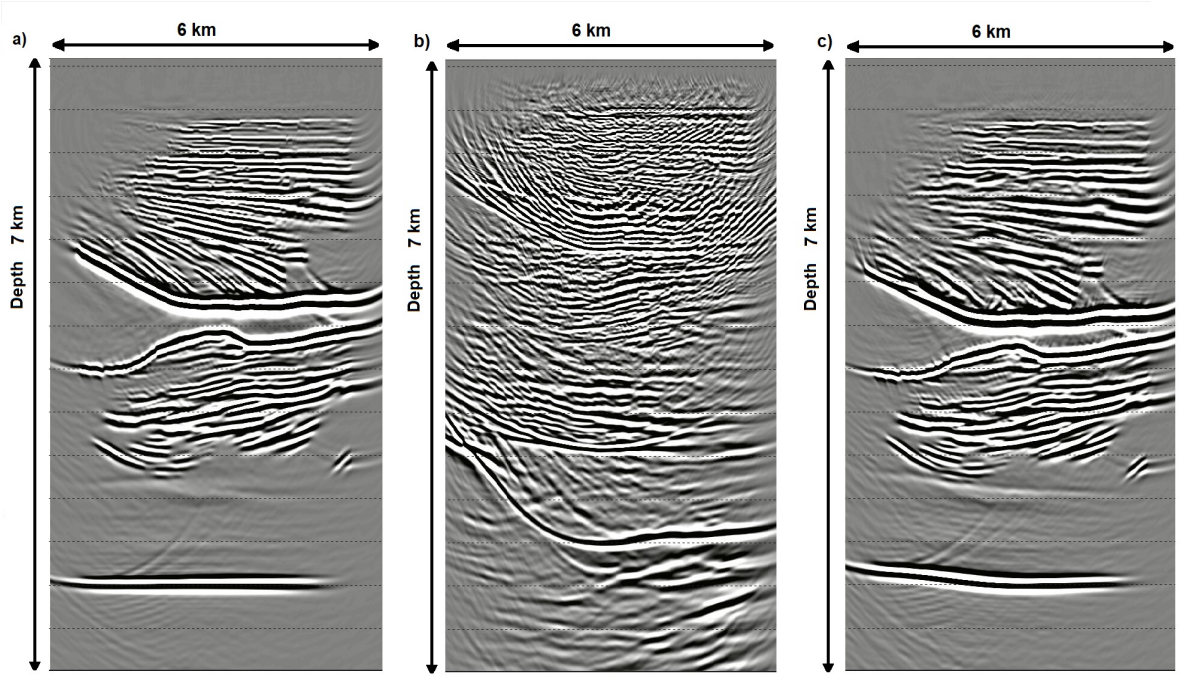

Fig. 13. Depth image obtained with PSDM using: (a) the exact velocity model; (b) the 1D initial velocity model; (c) the recovered velocity model obtained by tomography. A maximum offset of 4000 m was used in migration.

Field data example: ocean-bottom-cable data

We demonstrate this workflow using ocean-bottom-cable (OBC) seismic data. A zero-offset stack section is presented in Fig. 15a. CDP bin sampling in the stack is 25 m. The total number of CDPs in the line is 1,650, and the full size of the model in the inline direction is about 41 km. Fig. 14b shows the semblance maxima distribution obtained during slope estimation for each point in the stack section.

An initial velocity model was obtained by Dix conversion of stacking velocity volume subject to some spatial smoothing (Fig. 15a). The depth model dimensions are 41,250 x 5,000 m resulting in 1,650 x 500 grid points (X, Z) with a vertical sampling of 10 m and a horizontal sampling of 25 m. The input parameters of the tomographic inversion are as follows. Model grid discretization is Z = 100 m, X = 500 m. One fixed smoother loop has been used with window apertures equal to X = 12,000 m and Z = 3,000 m. The number of LSQR iterations is 20, whereas the number of IRLS (outer) iterations is 10. The results after ten nonlinear global iterations are presented in Fig. 15b. The difference between initial and estimated models is shown in Fig. 15c.

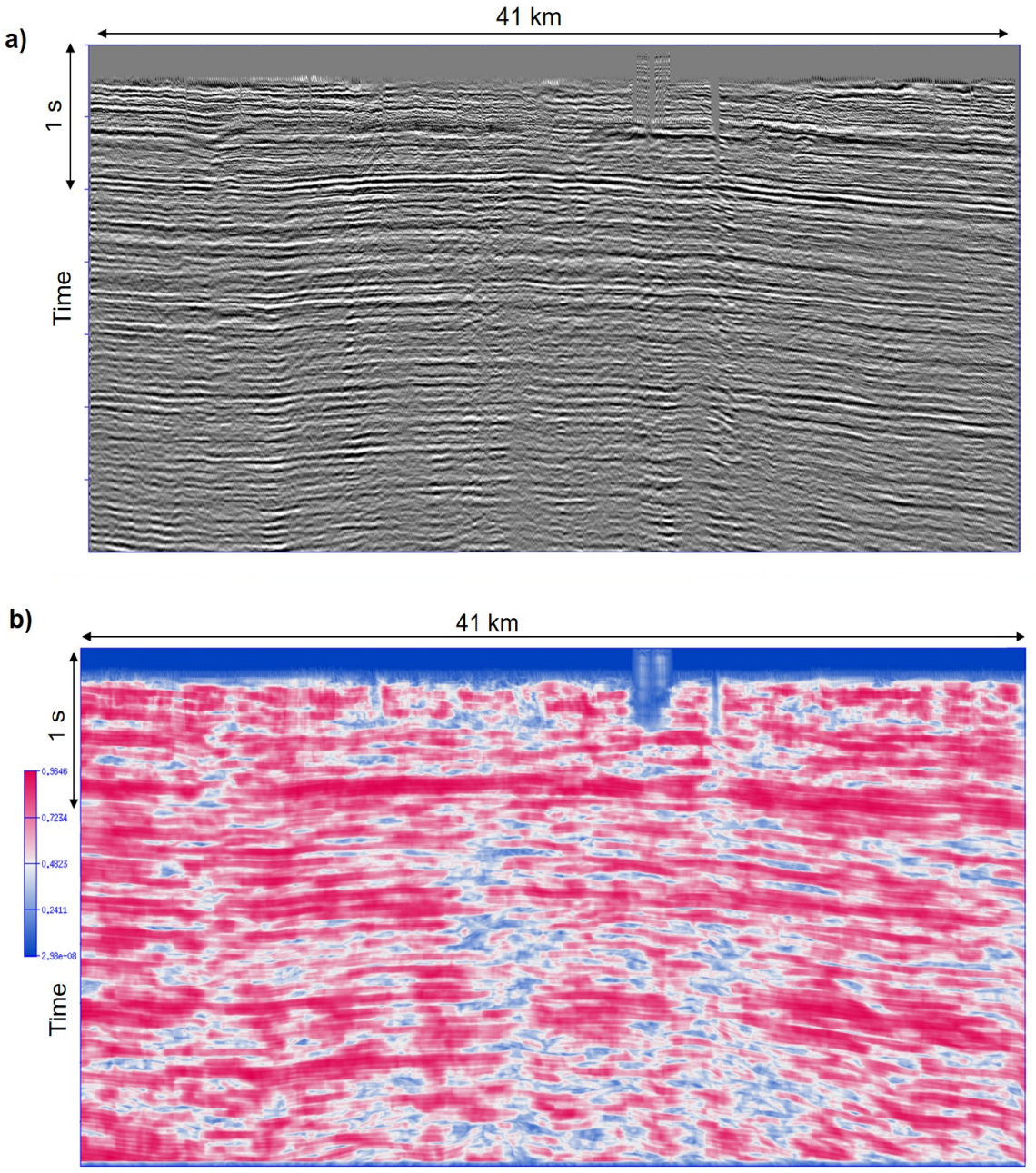

Fig. 14. (a) Stack section (narrow-azimuth data) used for the picking of local coherent events. (b) Maximum semblance distribution after picking local events in the stack section. The spatial aperture used for computing the semblance is 600 m.

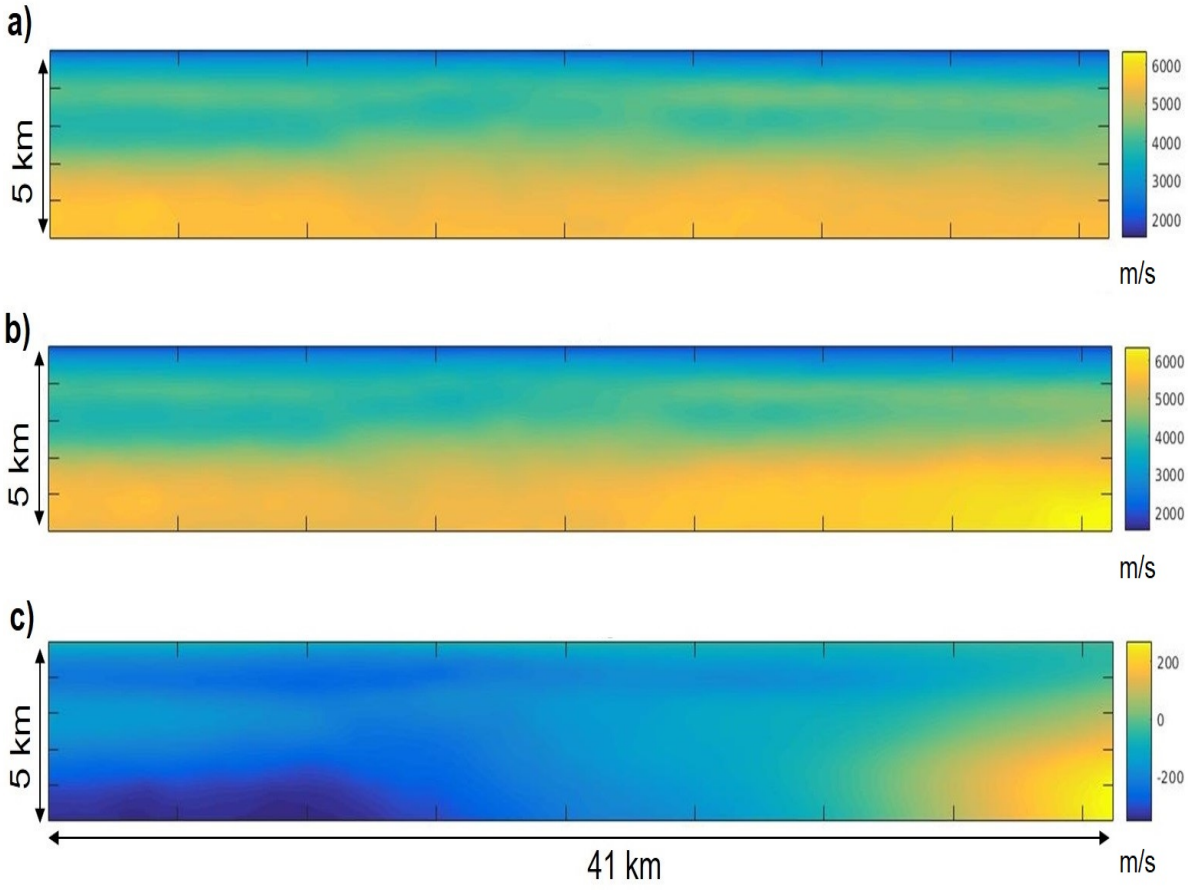

Fig. 15. Initial velocity model (a), estimated model after ten nonlinear iterations (b), and the difference between the two models (c) highlighting main areas of the tomographic update.

In Fig. 16, we compare depth images obtained using full-azimuth data. Clearly, the depth image with the tomographically recovered velocity model shows higher vertical resolution with more continuous events throughout the entire section compared to events imaged using the initial model (Fig. 16). Some events completely blurred on the original image become visible (red arrows in Fig. 16). The corresponding common-image gathers (CIGs) in Fig. 17 show flatter events with significantly reduced residual moveout when migrated with the final velocity model as opposed to the initial one, validating that tomography has successfully achieved its objectives.

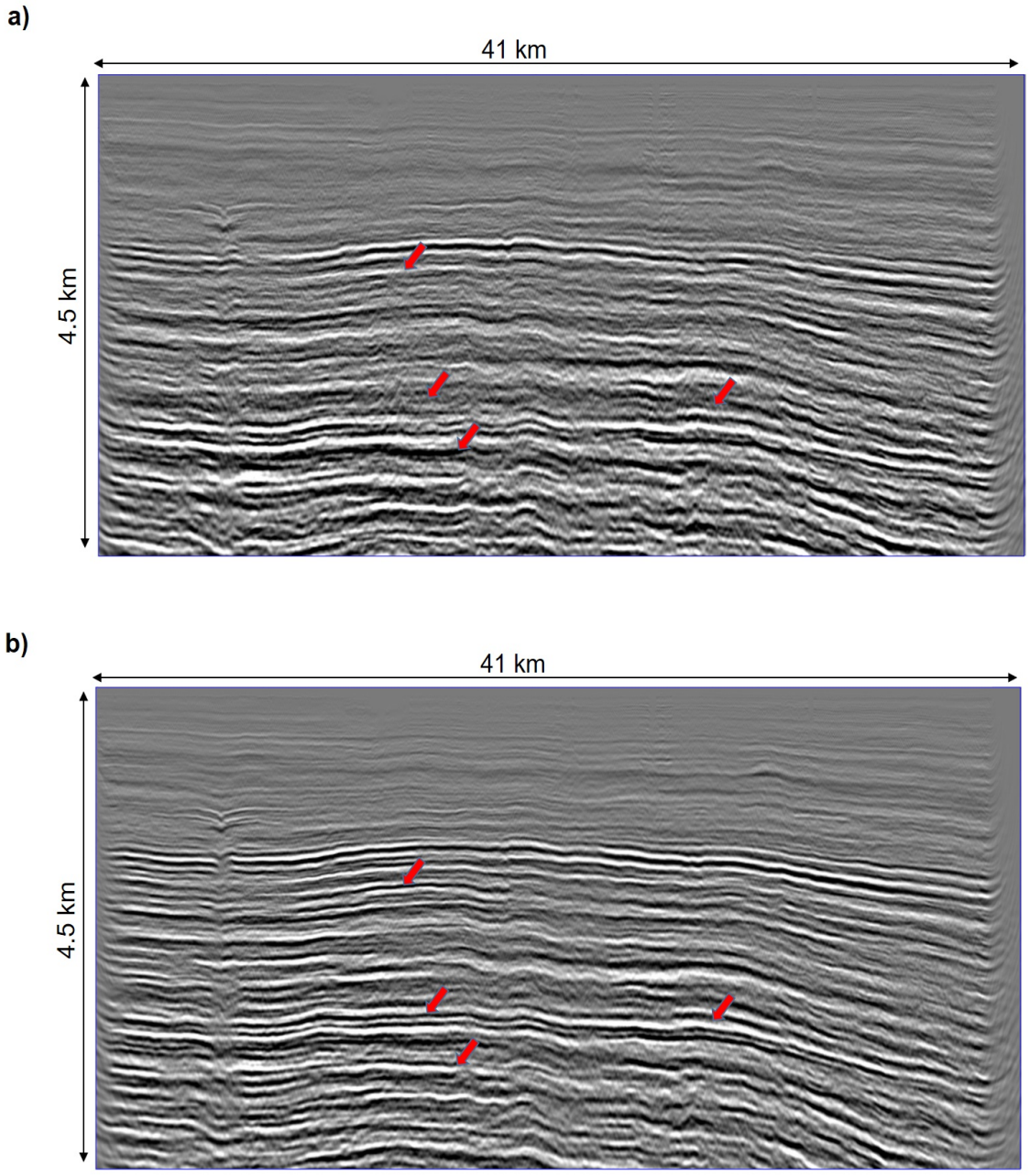

Fig. 16. Kirchhoff depth migration image obtained with the initial velocity model (a) and final recovered velocity model from tomography (b).

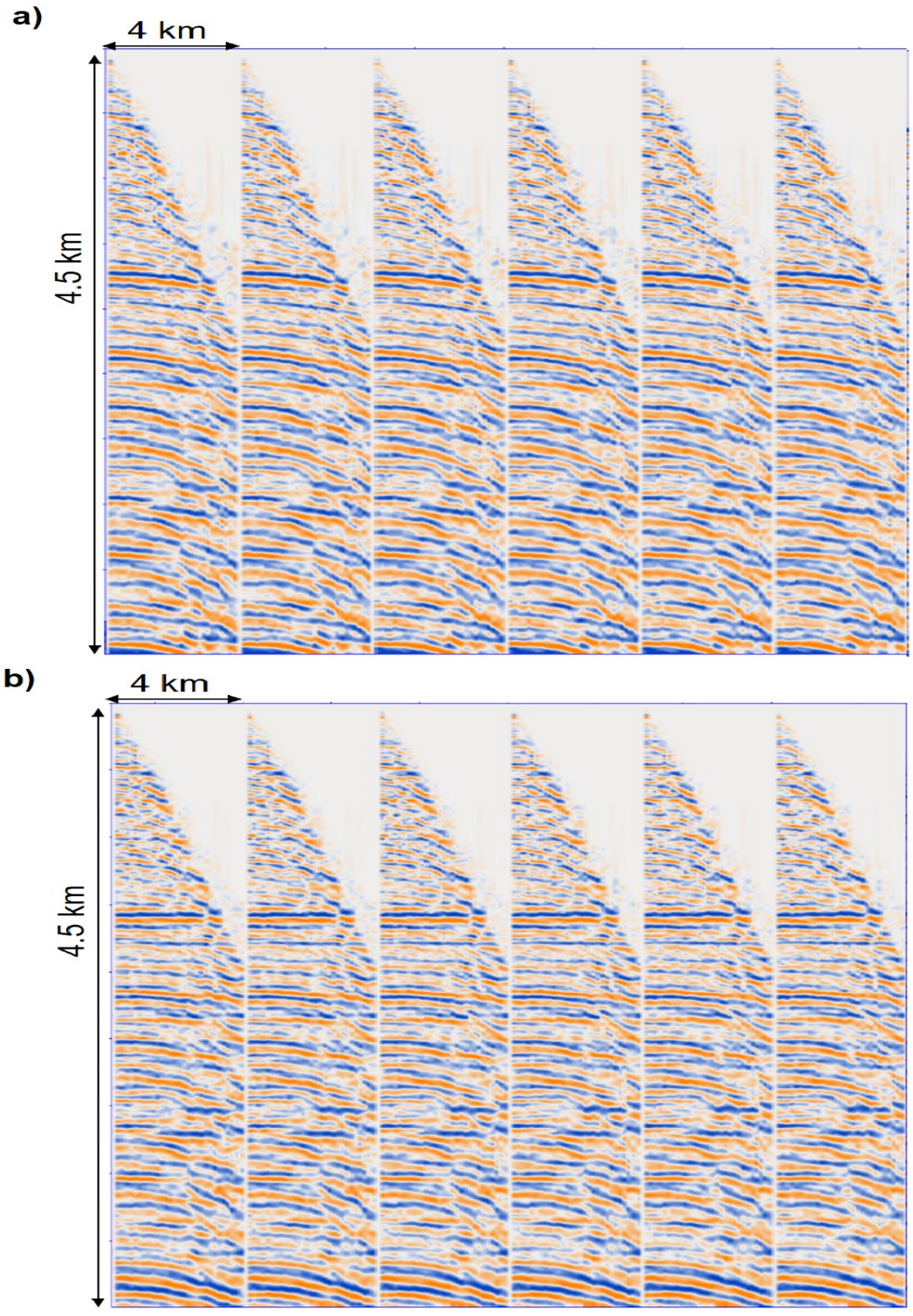

Fig. 17. Prestack common-image gathers obtained with Kirchhoff depth migration using the initial velocity model (a) and recovered velocity model from tomography (b).

CONCLUSION AND DISCUSSION

We developed a data-domain tomographic workflow coupled with a data-driven prestack data enhancement approach to robustly retrieve a reliable velocity depth model during an early stage of seismic processing. Such a model could serve as an initial velocity model for standard common-image-point tomography, MVA, or FWI. Besides, it may be the only model available for advanced iterative processing required to condition such data for subsequent velocity model building and imaging. The advantages of the proposed algorithm are the following: 1) there is no need for preliminary manual interpretation of seismic volumes since the algorithm is fully automatic and based on grid reflection tomography, 2) there is no need for computationally expensive two-point or dynamic raytracing, and 3) it is much cheaper computationally than standard common-image point tomography in the image domain.

Conventional MVA hinges on improved SNR of migrated gathers to perform robust picking of residual moveout. Also, in the image domain, the kinematics of primary reflected events differs from other events' kinematic, including multiples. Our data-domain approach improved data quality (prestack and poststack) by robust data enhancement with nonlinear beamforming. NLBF provides acceptable SNR for robust picking of the events in the poststack domain of our tomographic workflow. We may also appropriately tune the data enhancement approach's parameters to enhance only primarily reflected events required for the robust image as well as picking of poststack events and reliable prestack NMO velocities. Other events are suppressed, and the algorithm does not pick them. Also, instead of picking prestack traveltimes of reflected events for each offset, we utilize hyperbolic NMO approximation directly in the data domain; therefore, multiples and other events are further excluded or de-emphasized. However, for the data where multiples have a strong influence, the de-multiple procedures may be required.

The proposed data-domain approach can be effectively applied to recover an initial depth velocity model using challenging land and marine data with a low signal-to-noise ratio during the early stages of seismic processing. Such a technique enables iterative depth processing often required for such data. Real data examples confirm that depth images using an updated velocity model are more focused, and the flattening of the corresponding common-image gathers is improved.

REFERENCES

Al-Chalabi, M., 1973. Series approximation in velocity and traveltime computations. Geophys. Prosp., 21: 783-795.

Alkhalifah, T., 1997. Velocity analysis using nonhyperbolic moveout in transversely isotropic media. Geophysics, 62: 1839-1854.

Bakulin, A., Silvestrov, I., Dmitriev, M., Neklyudov, D., Protasov, M., Gadylshin, K., and Dolgov, 2020. Nonlinear beamforming for enhancement of 3D prestack land seismic data. Geophysics, 85 (3)**:** 1MJ-Z13.

Bakulin, A., Dmitriev, M., Silvestrov, I., Neklyudov, D., Gadylshin, K. and Protasov, P., 2018a. Efficient prestack enhancement based on local stacking: finding optimal domain for modern 3D land-seismic data. Expanded Abstr., 88th Ann. Internat. SEG Mtg., Anaheim: 4598-4602.

Bakulin, A., Silvestrov, I., Dmitriev, M., Neklyudov, D., Protasov, M., Gadylshin, K., Tcheverda, V. and Dolgov, V., 2018b. Nonlinear beamforming for enhancing prestack data with challenging near surface or overburden. First Break, 36(12): 121-126.

Bakulin, A. and Erickson, K., 2017. Enhance-estimate-image: New processing approach for single-sensor and other seismic data with low prestack signal-to-noise ratio. Expanded Abstr., 87th Ann. Internat. SEG Mtg., Houston: 5001-5005.

de Bazelaire, E., 1988. Normal moveout revisited - inhomogeneous media and curved interfaces. Geophysics, 53: 143-157.

Baykulov, M. and Gajewski, D., 2009. Prestack seismic data enhancement with partial common-reflection-surface (CRS) stack. Geophysics, 74(3): V49-V58.

Berkovitch, A., Deev, K. and Landa, E., 2011. How non-hyperbolic multifocusing improves depth imaging. First Break, 27: 95-103.

Billette, F. and Lambaré, G., 1998. Velocity macro-model estimation by stereotomography. Geophys. J. Internat., 135: 671-680.

Buzlukov, V. and Landa, E., 2013. Imaging improvement by prestack signal enhancement. Geophys. Prosp., 61: 1150-1158.

Castle, R.J., 1988. Shifted hyperbolas and normal moveout. Expanded Abstr., 58th Ann. Internat. SEG Mtg., Anaheim: S9.3.

Chauris, H., Noble, M.S., Lambaré, G. and Podvin, P., 2002. Migration velocity analysis from locally coherent events in 2D laterally heterogeneous media - Part I: Theoretical aspects. Geophysics, 67: 1202-1212.

Duveneck, E., 2004. Tomographic determination of seismic velocity models with kinematic wavefield attributes. Logos Verlag, Berlin.

Duveneck, E., 2004. Velocity model estimation with data-derived wavefront attributes. Geophysics, 69: 265-274.

Dümmong S., Meier, K., Gajewski, D. and Hübscher, C., 2008. Comparison of prestack stereotomography and NIP wave tomography for velocity model building: Instances from the Messinian evaporates. Geophysics, 73(5): VE291-VE302.

Fagin S., 1999. Model Based Depth Imaging. SEG, Tulsa, OK.

Fehmers, G.C. and Höcker, C.F.W., 2003. Fast structural interpretation with structure-oriented filtering. Geophysics, 68: 1286-1293.

Guillaume, P., Lambaré, G., Leblanc, O., Mitouard, P., Moigne, K., Montel, J., Prescott, T., Siliqi, R., Vidal, N., Zhang, X. and Zimine, S., 2008. Kinematic invariants: an efficient and flexible approach for velocity model building. Expanded Abstr., 88th Ann. Internat. SEG Mtg., Anaheim.

Guiziou, J.L., Mallet, J.L. and Madariaga, R., 1996. 3D seismic reflection tomography on top of the GOCAD depth modeler. Geophysics, 61: 1499-1510.

Gjoystdal, H. and Ursin, B., 1981. Inversion of reflection times in three dimensions. Geophysics, 46: 972-983.

Hubral, P. and Krey, T., 1980. Interval Velocities from Seismic Reflection Time Measurements. SEG, Tulsa, OK.

Jones, I.F., 2004. A review of 3D PreSDM model building techniques. First Break, 21: 41-54.

Jones, I.F., 2010. An Introduction to Velocity Model Building. EAGE, Houten, Netherlands.

Klüver, T., 2006. Velocity model building using migration to residual time. Expanded Abstr., 88th Ann. Internat. SEG Mtg, Anaheim: 2022-2026.

Lambaré, G., 2008. Stereotomography. Geophysics, 73(5): VE25-VE34.

Lambaré, G., Guillaume, P. and Montel, J.P., 2014. Recent advances in ray-based tomography. Extended Abstr., 76th EAGE Conf., Amsterdam: We G103 01.

Lavaud, B., Baina, R. and Landa, E., 2004. Automatic robust velocity estimation by poststack stereotomography. Expanded Abstr., 74th Ann. Internat. SEG Mtg., Denver: 2351-2354.

Van der Made, P.M., van Riel, P. and Berkhout, A.J., 1987. Estimation of complex velocity models from stacking information. Expanded Abstr., 57th Ann. Internat. SEG Mtg., New Orleans: 821-823.

Neckludov, D., Baina, R. and Landa, E., 2006. Residual stereotomographic inversion. Geophysics, 71(4): E35-E39.

Paige, C.C. and Saunders, M.A., 1982. LSQR: An algorithm for sparse linear equations and sparse least squares. ACM Transact. Math. Software, 8: 43-71.

Rakotoarisoa, H., Guillaume, P., Blondel, P.C. and Charles, S., 1995. An adapted geometrical criterion for 3-D tomographic inversion. Expanded Abstr., 88th Ann. Internat. SEG Mtg., Anaheim: 1062-1065.

Rauch-Davies, M., Berkovitch, A., Deev. K. and Landa, E., 2013. Non-hyperbolic multifocusing imaging for prestack signal enhancement. Expanded Abstr., 83rd Ann. Internat. SEG Mtg., Houston: 4618-4622.

Robein, E., 2010. Seismic Imaging: A Review of the Techniques, their Principles, Merits and Limitations. EAGE, Houten, Netherlands.

Scales, J., Gersztenkorn, A. and Treitel, S., 1988. Fast Ip solution of large, sparse linear systems, application to seismic traveltime tomography. J. Comput. Phys., 75: 313-333.

Sexton, P.A., 1998. 3D velocity-depth model building using surface seismic and well data (SuperDix). Ph.D. Thesis, University of Durham., Durham.

Sexton, P. and Williamson, P., 1998. 3D Anisotropic velocity estimation by model-based inversion of prestack traveltimes. Expanded Abstr., 68th Ann. Internat. SEG Mtg., New Orleans:1855-1858.

Tanushev, N., Popovici, A. and Hardesty, S., 2017. Fast, high-resolution beam tomography and velocity-model building. The Leading Edge, 36: 140-145.

Tsvankin, I. and Thomsen, L., 1994. Nonhyperbolic reflection moveout in anisotropic media. Geophysics, 59: 1290-1304.

Woodward, V., Nichols, D., Zdraveva, O., Whitfield, P. and Johns, T., 2008. A decade of tomography. Geophysics, 73(5): VE5-VE11.

Yilmaz, Ö., 2001. Seismic Data Analysis: Processing, Inversion, and Interpretation of Seismic Data. SEG, Tulsa, OK.

Xie, Y., 2017. 3D prestack data enhancement with a simplified CO CRS. Extended Abstr., 79th EAGE Conf., Paris: WeP7.13